NANO · MICRO
small
www.small-journal.com

Active Interphase Enables Stable Performance for an All-Phosphate-Based Composite Cathode in an All-Solid-State Battery

Qi Xu, Zigeng Liu, Anna Windmüller, Shibabrata Basak, Junbeom Park, Krzysztof Dzieciol, Chih-Long Tsai, Shicheng Yu, Hermann Tempel, Hans Kungl, and Rüdiger-A. Eichel*

High interfacial resistance and unstable interphase between cathode active materials (CAMs) and solid-state electrolytes (SSEs) in the composite cathode are two of the main challenges in current all-solid-state batteries (ASSBs). In this work, the all-phosphate-based $LiFePO_4$ (LFP) and $Li_{1.3}Al_{0.3}Ti_{1.7}(PO_4)_3$ (LATP) composite cathode is obtained by a co-firing technique. Benefiting from the densified structure and the formed redox-active $Li_{3-x}Fe_{2-x-y}Ti_xAl_y(PO_4)_3$ (LFTAP) interphase, the mixed ion- and electron-conductive LFP/LATP composite cathode facilitates the stable operation of bulk-type ASSBs in different voltage ranges with almost no capacity degradation upon cycling. Particularly, both the LFTAP interphase and LATP electrolyte can be activated. The cell cycled between 4.1 and 2.2 V achieves a high reversible capacity of 2.8 mAh cm^{-2} (36 µA cm^{-2}, 60 °C). Furthermore, it is demonstrated that the asymmetric charge/discharge behaviors of the cells are attributed to the existence of the electrochemically active LFTAP interphase, which results in more sluggish Li^+ kinetics and more expansive LFTAP plateaus during discharge compared with that of charge. This work demonstrates a simple but effective strategy to stabilize the CAM/SSE interface in high mass loading ASSBs.

1. Introduction

With the increasing demand for safe operation, high energy density and long cycle life lithium-ion batteries, all-solid-state batteries (ASSBs) are becoming one of the most promising next generation electrochemical storage systems to replace the conventional lithium-ion batteries, which employ organic liquid electrolytes.[1] Nevertheless, many issues still need to be resolved before ASSBs can compete against the state-of-art batteries in energy density and cost effectivity. Interfacial issues including high interfacial resistance and unstable interphase between cathode active materials (CAMs) and solid-state electrolytes (SSEs) are among the major challenges, hindering the electrochemical performance and commercialization of ASSBs.[2–5]

The interface between heterogeneous particles of SSE and CAM is a region where the structural (crystal structure and defect density), chemical (composition and ion concentration), and electrical (ionic and electronic conductivities) properties change from one side to the other.[6–8] During the processing of composite cathode, the interface of CAM/SSE might be modified by a new phase (cathode electrolyte interphase) due to elemental inter-diffusion and/or interfacial chemical reaction.[8–10] A suitable interphase should have the following features: good (electro) chemical compatibility with both the CAM and SSE, sufficient ionic conductivity at the operation temperature and high structural and mechanical stability within the operating voltages of the cell.[6,11,12] It is reported that enhancing the ionic conductivity of the interphase between CAM and SSE facilities fast interfacial Li^+ kinetics and boosts the electrochemical performance of ASSBs.[13–15] Wang et al. showed that the ionic conductivity of the $LiNb_{0.5}Ta_{0.5}O_3$ (LNTO) interphase layer on the surfaces of $LiNi_{0.5}Mn_{0.3}Co_{0.2}O_2$ determined the electrochemical performance of the LNTO-coat $LiNi_{0.5}Mn_{0.3}Co_{0.2}O_2|Li_{10}GeP_2S_{12}|LiIn$ solid-state cell.[15] Specifically, the $LiNi_{0.5}Mn_{0.3}Co_{0.2}O_2$ coated by the highest Li^+ conductive LNTO exhibited accelerated interfacial Li^+ transportation, enabling the ASSB to achieve high specific capacities of 152 and 107.5 mAh g^{-1} at 0.1C and 1C (room temperature), respectively.

Q. Xu, Z. Liu, A. Windmüller, S. Basak, J. Park, K. Dzieciol, C.-L. Tsai, S. Yu, H. Tempel, H. Kungl, Rüdiger-A. Eichel
Forschungszentrum Jülich, Fundamental Electrochemistry (IEK-9)
D-52425 Jülich, Germany
E-mail: s.yu@fz-juelich.de

Q. Xu, Rüdiger-A. Eichel
Institute of Physical Chemistry
RWTH Aachen University
D-52074 Aachen, Germany

S. Basak
Forschungszentrum Jülich, Ernst Ruska-Centre for Microscopy and Spectroscopy with Electrons (ERC)
D-52425 Jülich, Germany

Rüdiger-A. Eichel
Forschungszentrum Jülich, Helmholtz Institute Münster: Ionics in Energy Storage (IEK-12)
D-48149 Münster, Germany

The ORCID identification number(s) for the author(s) of this article can be found under https://doi.org/10.1002/smll.202200266.

DOI: 10.1002/smll.202200266

Strategies for designing stable and ion-conductive interphase in the composite cathode are highly dependent on the material combinations. Attention needs to be paid to the chemical and electrochemical compatibilities of the used CAM and SSE. In general, the reactivity of oxide-/phosphate-based SSEs against CAMs is lower compared with that of sulfide-based SSEs.[16,17] However, oxide-/phosphate-based SSEs are typically rigid ceramics with low elasticities and high bond dissociation energies, making them difficult to form intimate contacts with CAM.[6,18] Insufficient contact and high porosity between CAM and SSE can lead to a high tortuosity for ion-conduction and a loss of contact to the active sites in the composite cathode, which substantially limit the electrochemical performance of the ASSBs.[19,20] In order to form sufficient interfacial adhesion between oxide-/phosphate-based SSEs and CAMs, the processing temperatures of the composite cathodes are usually quite high. This might induce side reactions because of the accelerated elemental inter-diffusion. Literature showed that the elemental inter-diffusion in thermally unstable CAM/SSE combinations caused decompositions of CAM or SSE where the decomposed byproducts acted as insulating phases, strongly impeding the Li^+ transportation.[16,19,21–25] Thus, thermal and chemical compatibilities of CAM/SSE at the processing temperature and (electro)chemical properties of the CAM/SSE interphase are the determining factors for the choice of CAM/SSE combinations.

Phosphate-based NASICON-type $Li_{1.3}Al_{0.3}Ti_{1.7}(PO_4)_3$ (LATP) is attractive to be employed as the SSE for ASSBs due to its competitive ionic conductivities and good chemical stability in ambient atmosphere.[26–28] LATP is considered to have better thermal stability with phospho-olivine $LiMPO_4$ (M: Fe, Mn, Co, Ni) cathodes because the oxygen atoms are tightly bound to P with the strong covalent bonds in both LATP and $LiMPO_4$.[29] It was reported that the mixture of LATP and different phosphate-based CAMs such as $LiFePO_4$ (LFP), $LiCoPO_4$, and $LiMn_{0.5}Fe_{0.5}PO_4$ showed promising thermal stabilities at elevated sintering temperatures around 700—800 °C in an inert atmosphere.[30] In particular, the co-fired LFP/LATP exhibited the most promising result, forming only a small fraction of NASICON-type $Li_2FeTi(PO_4)_3$ interphase.[30] NASICON-type compound is intrinsically an ion-conductor,[31] which is desired to be employed as the cathode electrolyte interphase. In addition, Rao et al. showed improved ionic conductivity of $LiTi_2(PO_4)_3$ when partial Ti^{4+} is substituted by trivalent Fe^{3+} with the composition of $Li_{1+x}Ti_{2-x}Fe_x(PO_4)_3$ ($x = 0.05$, 0.1, and 0.15).[32] In particular, $Li_{1.15}Ti_{1.85}Fe_{0.15}(PO_4)_3$ achieved ionic conductivity of 0.52 mS cm^{-1} at room temperature, which is comparable with that of LATP.[26,32–34] Apart from their decent ionic conductivities, NASICON-type $LiM_2(PO_4)_3$ materials consisting of transition metal ions are redox-active.[35–37] Patoux et al. demonstrated the reversible Li^+ insertion/extraction of NASICON-type $Li_2FeTi(PO_4)_3$ using the potentiostatic intermittent titration technique.[35]

Although the good thermal stability of LATP against LFP has been proved previously,[30,38] the electrochemical performance of ASSBs made from their composite cathodes has barely been reported. The major issue lies in the fact that the densification temperatures of LATP prepared by conventional synthesis methods are still too high (1000 °C) to circumvent the decomposition reactions of LFP and/or LATP.[30,33] In our previous work, highly ionically conductive LATP can be obtained at a low sintering temperature of 775 °C with the help of liquid phase sintering.[34] The reduced densification temperature of LATP is considered to have the ability to suppress the decomposition of LFP/LATP during the co-firing process. On the other hand, like many CAMs, the redox-reaction of electrochemically active interphase influences its ionic conductivity,[39,40] affecting the Li^+ transport kinetics and electrochemical behavior of the ASSB. Although the effects of a redox-active interphase on the electrochemical performance of ASSBs are reported for composite cathodes by using sulfide-based SSEs,[41–44] little information can be found for oxide/phosphate-based composite cathodes.

In this work, highly compacted all-phosphate composite cathodes with the industrial relevant areal capacities of 2.0–3.0 mAh cm^{-2} were fabricated by co-firing the self-prepared LATP and commercially available carbon coated LFP powders in Ar atmosphere at 775 °C. LFP is chosen due to its high safety, relatively low price, and good thermal stability combined with LATP.[30,38,45] Chemical structural, microstructural, and electrical properties of the co-fired LFP/LATP composite cathode were characterized. Electrochemical performances of ASSBs made from the co-fired LFP/LATP composite cathodes were investigated and analyzed. Moreover, the influence of the Li^+ transport kinetic of the redox-active interphase on the battery performance was studied.

2. Results and Discussion

2.1. Characterization of the Co-fired LFP/LATP Composite Cathode

Since the oxidation of Fe^{2+} in LFP to Fe^{3+} starts at 300 °C in ambient atmosphere (Figure S1, Supporting Information), the LFP/LATP composite cathode was co-fired in Ar atmosphere at 775 °C for 2 h to achieve a high relative density around 90%.

2.1.1. Structural Properties of LFP, LATP, and Co-Fired LFP/LATP Samples

Individual components of LFP and LATP were sintered in Ar atmosphere at 775 °C and analyzed by powder X-ray diffraction (XRD) to exclude the effects of the thermal and atmospheric impacts on the structural stabilities of LFP and LATP. Then, XRD measurement was performed on the co-fired LFP/LATP sample to analyze its phase composition. The phase compositions, lattice parameters, unit cell volumes, and weight percentages of each phase obtained by the Rietveld method are listed in Table S1, Supporting Information.

For LATP sintered in Ar, as presented in **Figure 1**a, apart from the pre-dominant rhombohedral NASICON-type LATP phase in the $R\bar{3}c$ space group (ICSD code: 257190), a secondary phase belonging to a variant of NASICON polymorphs with orthorhombic structure in the *Pbna* space group is formed.[46] It is worth noting that the standard $Li_2FeTi(PO_4)_3$ XRD pattern (ICSD code: 151919) was used as the reference *Pbna* phase

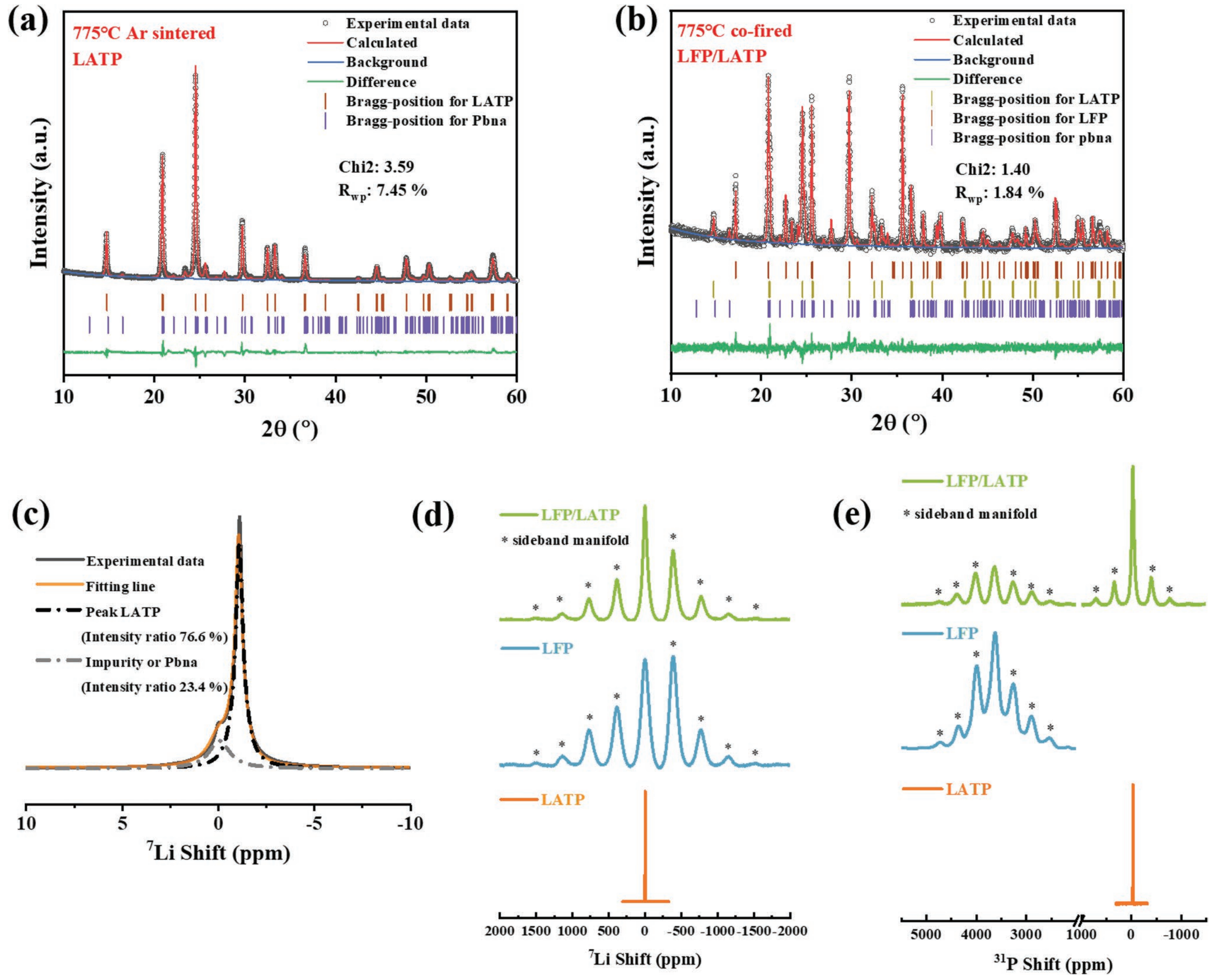

Figure 1. XRD patterns and refinement results of the 775 °C Ar sintered a) LATP and b) LFP/LATP. c) ^{7}Li MAS-NMR spectra of the 775 °C Ar sintered LATP, where Chi2 (Chi squared) and R_{wp} (weighted profile residual) represent the quality of fitting. Comparison of d) ^{7}Li and e) ^{31}P MAS-NMR spectra of the 775 °C Ar sintered LATP, LFP, and LFP/LATP.

for the Rietveld refinement because the *Pbna* phase only containing LATP elements is not available in ICSD database. The refinement results show that the lattice constant c (20.8774 Å) of LATP is larger than that of the reported LATP sintered in air (20.8143 Å) (Table S1, Supporting Information),[34] suggesting the obtained rhombohedral LATP has a higher Ti/Al ratio due to the larger ionic radius of Ti^{4+} (60.5 pm, coordination: 6) compared with that of Al^{3+} (53.5 pm, coordination: 6).[47] This agrees with what Gellert et al. have observed that heat treatment of $Li_{1.5}Al_{0.5}Ti_{1.5}(PO_4)_3$ in Ar/H_2 atmosphere leads to an Al^{3+} deficient LATP due to the formation of $AlPO_4$.[30] Besides, the structure transition from rhombohedral to orthorhombic NASICON was reported for $Li_{1+x}In_xTi_{2-x}(PO_4)_3$ and $Li_{1+y}Fe_yTi_{2-y}(PO_4)_3$ when $0.4 < x \leq 1.0$ and $y > 0.6$, respectively,[48,49] indicating that extensive doping of trivalent ions in $LiTi_2(PO_4)_3$ results in this phase transition. Attention needs to be paid that the used intermediate LATP powders in our work were prepared with an excess of Li by 10 wt%, which implies the formation of Al- and Li-rich orthorhombic NASICON-like *Pbna* phase could be attributed to the synergic effects of Al^{3+} inhomogeneous distribution and Li-excess.[30,50] As both LATP phases contain similar elements but are only different in stoichiometry, we name the NASICON-type rhombohedral and orthorhombic phases as r-LATP and o-LATP, respectively. Unlike LATP, LFP maintains the structural integrity after sintering in Ar, evidenced by the monophase composition (ICSD code: 97764) and the nearly unchanged lattice parameters compared with those of the literature data (Figure S2a and Table S1, Supporting Information).[51]

Figure 1b shows the XRD pattern of the co-fired LFP/LATP, in which three different phases that belong to olivine-type LFP, r-LATP and o-LATP are identified. The Rietveld refinement results show that the lattices parameters of LFP in the co-fired LFP/LATP and the sintered LFP are comparable (Table S1, Supporting Information). It is noticed that the *Pbna* phase in the co-fired LFP/LATP sample takes a much higher weight percentage (22.3 wt%) than that of the physical mixtures of individually sintered LFP and LATP (9.0 wt%) (Figure S2b and Table S1, Supporting Information). These results suggest that the olivine LFP phase is not likely to be doped by a large amount of Ti^{4+}/Al^{3+} ions, which have significantly smaller ionic radii compared with that of Fe^{2+} (78.0 pm, coordination: 6). On the other hand, attributed to elemental inter-diffusion, the co-firing process promotes the phase transition of LATP from r-LATP to o-LATP. The larger unit cell volume of *Pbna* phase in the co-fired LFP/LATP sample (864.0 Å^3) than that in the LATP sample (862.8 Å^3) indicates that Fe^{2+} replaces partial Ti^{4+} and/or Al^{3+} sites in LATP to form a high fraction of Fe-doped o-LATP at the LFP/LATP interface.[47] As XRD can only give us an averaged unit cell volume of the o-LATP in the co-fired LFP/LATP, the chemical composition quantification of the formed interphase cannot be achieved. Thus $Li_{3-x}Fe_{2-x-y}Ti_xAl_y(PO_4)_3$ ($0 \le x + y \le 2$, LFTAP) is proposed as the overall interphase chemical composition.

Magic-angle spinning (MAS) nuclear magnetic resonance (NMR) spectroscopy was performed to investigate the local chemical environment of the Ar atmosphere sintered LATP, LFP, and co-fired LFP/LATP (Figure 1c–e). As demonstrated in Figure 1c, the formation of o-LATP in LATP is also indicated by ^{7}Li MAS-NMR by obtaining a shoulder of the peak at –0.1 ppm aside from the main resonance at –1.1 ppm.[52] The intensity ratio of the peaks is 76.6 : 23.4, which agrees with the Rietveld refinement result that the o-LATP is present in 19.5 wt% in LATP (Table S1, Supporting Information). Besides, only one isotropic resonance is obtained for ^{31}P MAS-NMR (–28.4 ppm) and ^{27}Al MAS-NMR (–14.7 ppm) (Figure 1e; Figure S3, Supporting Information), indicating the difference in local environments for P and Al in r-LATP and o-LATP are negligible. The results suggest that the structure framework of r-LATP and o-LATP are similar, but the sites for mobile Li-ions are slightly different. Combining the NMR results with the XRD results of Ar sintered LATP, the reason might be o-LATP has a higher amount of AlO_6-octahedral and occupied Li-sites than those of r-LATP. For LFP, the ^{7}Li and ^{31}P MAS-NMR spectra have isotropic resonances at –1.0 ppm and 3624.4 ppm, respectively (Figure 1d,e). Both resonances can be assigned to monophasic LFP with wide spinning sideband (SSB) manifolds over 600 kHz. The large SSB manifolds are due to the strong dipolar interaction between the Fe^{2+} paramagnetic spins and Li/P nuclei.[53,54]

For the co-fired LFP/LATP, the ^{7}Li MAS NMR spectrum shows one isotropic resonance at 1.3 ppm with wide SSB manifolds (Figure 1d). The deconvolution of this isotropic resonance to LFP, r-LATP, and o-LATP contributions without detailed information on the lineshape for the different phases is impossible. The ^{31}P MAS NMR spectrum of the co-fired LFP/LATP shows two regions for LFP and LATP phases, respectively (Figure 1e). The similarity of ^{31}P resonance at the LFP region in the co-fired LFP/LATP sample and LFP sample suggests the local chemical environment for P in the LFP phase is hardly changed after the co-firing at 775 °C. It is further observed that the full width at half maximum for ^{7}Li, ^{31}P and ^{27}Al MAS NMR spectrum of the co-fired LFP/LATP are much larger than those for LATP, suggesting the Li-ions in different phases are all under the influence of paramagnetic centers of Fe^{2+} ions (Figure 1d,e; Figure S3, Supporting Information). These indicate the different phases in the composite cathode are closely connected while the unpaired electrons of the Fe^{2+} influence the local chemical environment for Li, P and Al in LATP phases dramatically. On the other hand, broader full width at half maximum also implies the partial substitution of Ti/Al by Fe in the LATP phases by the formation of Fe-doped NASICON-type LATP.

The morphology of co-fired LFP/LATP sample was investigated by using scanning electron microscopy (SEM) and scanning transmission electron microscopy (STEM) with energy dispersive X-ray analysis (EDX). The SEM images show that the co-fired LFP/LATP sample is compact with clearly two phases in the form of micron-sized grains (Figure S4b, Supporting Information). Determined by the EDX mapping of Ti, Al, and Fe in the STEM image, the light and dark-gray contrast particles in the SEM image are LFP and LATP, respectively (**Figure 2**a; Figure S4b, Supporting Information). It is worth noting that grain size of LFP after co-firing is roughly doubled compared with that of pristine LFP (Figure S4a,b, Supporting Information). The Ti, Al, and Fe elemental distributions for LFP, LATP particles and across their interfaces were further investigated by using the high magnification EDX analysis. As illustrated in Figure 2a, the elemental distribution of Fe in LFP and Ti, Al in LATP are quite homogeneous in their bulks, while different elemental inter-diffusion zones across the interface between LFP and LATP particles can be found. By examining the atomic percentage of Ti, Al and Fe from the EDX line scans across the LFP/LATP interfaces, different thicknesses of elemental inter-diffusion zones with Ti, Al, and Fe concentration gradients were determined (Figure 2b,c; Figure S5, Supporting Information). Some interfaces show relatively thin inter-diffusion zones of ≈40 nm (e.g., Line 1, Figure 2b), while thicker ones can be up to ≈100 nm (e.g., Line2, Figure 2c). When compared to the particle size of LFP and LATP (≈1 µm), a rough estimation suggests the elemental inter-diffusion zone taking up about 8–20% volume of the co-fired LFP/LATP sample, which is consistent with the XRD results.

To study the structural properties of the formed LFTAP interphase, high resolution transmission electron microscopy (HRTEM) was performed. Determined by the bright field TEM image, the dark and light-gray contrast particles should belong to LFP and LATP, respectively (Figure 2d). Figure 2e shows the interfacial region indicated in the TEM image (gray box in Figure 2d), which consists of three connected HRTEM images across the LFP/LATP interface. Lattice fringes of LFP and LATP are clearly present in the HRTEM images, indicating their high crystallinity (Figure 2e). The diffraction pattern of LFP region agrees well with olivine LFP in the *Pnma* space group (Figure S6b,f, Supporting Information). Further magnifying the HRTEM image in the LFP region, the interplanar spacing of 0.35 and 1.05 nm corresponding to the (1 1 1) and (1 0 0) lattice planes of LFP, respectively, are well recognized (Figure 2f).[55] In the LFP/LATP interfacial region, diffraction patterns of LFP and LATP are overlapped (Figure S6c,d,g,h, Supporting Information). Nevertheless, they suggest the observed LATP (Figure 2d) belongs to o-LATP in the *Pbna* space group. Accordingly, the magnified HRTEM images show interplanar spacings of 0.32 and 1.13 nm, matching well with the (2 1 2) and (0 0 1) lattice planes of *Pbna* phase, respectively (Figure 2g,h). It needs to be mentioned that the LATP particle which is not in direct contact with LFP (Figure S6a, Supporting Information) shows

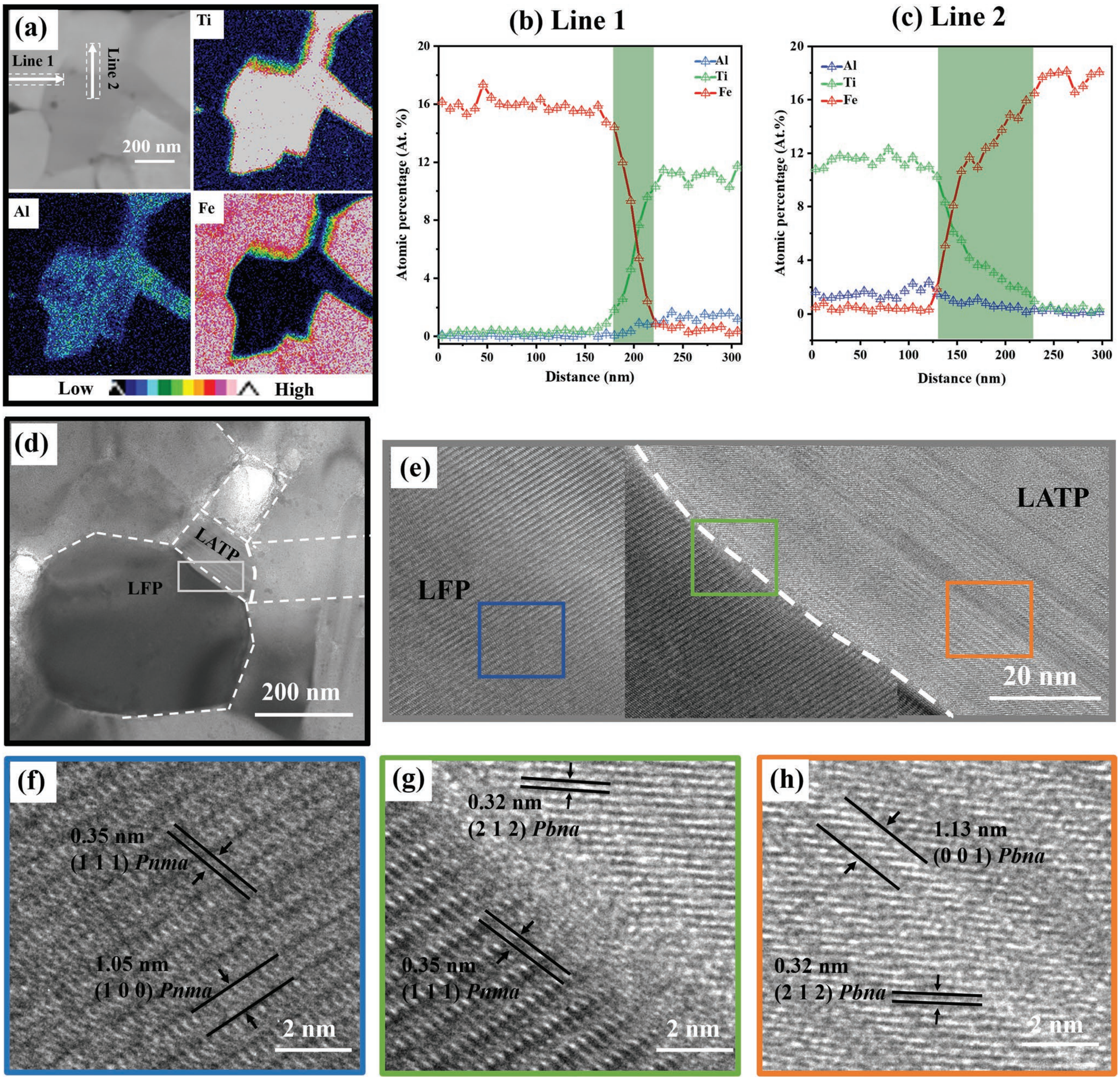

Figure 2. Microstructural analysis of the co-fired LFP/LATP. a) STEM image and corresponding elemental mapping of Fe, Ti, and Al (low/high color bar represents the atomic intensity of the relevant element). b,c) Fe, Ti, and Al atomic percentage distributions across the LFP/LATP interface (line positions are indicated in (a)). d) TEM image and e) HRTEM image (a connection of three HRTEM images) from the gray box shown in (d). Magnified HRTEM images from the f) blue, g) green, and h) orange boxes are shown in (e), respectively.

the structure of r-LATP in the $R\overline{3}c$ space group. This validates that the phase transition of LATP is preferentially to take place near the LFP/LATP interface because of the incorporation of Fe-ions in LATP lattice (Figure S6a,e,i, Supporting Information). These results agree well with the previous discussion that the diffusion of Fe into LATP structure may trigger the phase transition of LATP from r-LATP to Fe-doped o-LATP (LFTAP).[49]

More TEM and HRTEM images in a different area of the co-fired LFP/LATP sample are demonstrated in Figure S7, Supporting Information. The results are comparable with those of the above measurement that the *Pbna* phase is formed at the interfacial region between LFP and LATP. Further HRTEM measurements were performed on pristine and Ar sintered LFP powders to check the influence of the sintering process on the carbon coating of the used LFP. They show that carbon coating is not affected after heating the pristine LFP in Ar because amorphous carbon layers are identified in both the pristine and Ar sintered LFP powder samples (Figure S8a,b, Supporting Information). Whereas, for the co-fired LFP/LATP, carbon layers are only observed on those surface regions of LFP particles where they were not attached to LATP (Figure S8c, Supporting Information). This indicates that the carbon on the LFP/LATP interfacial regions might react and be released as gas phases. In this scenario, the carbon is partially oxidized and to maintain charge neutrality, a minor reduction of the Ti^{4+} to Ti^{3+} at the LFP/LATP interface is expected.

2.1.2. Electrical Properties of the Co-Fired LFP/LATP Composite Cathode

The total ionic and electronic conductivities of the co-fired LFP/LATP sample (σ_i and σ_e, respectively) were determined by using electrochemical impedance spectroscopy (EIS) in the temperature range of 50–150 °C. **Figure 3**a displays a typical Nyquist plot of the co-fired LFP/LATP sample measured at 60 °C. It is acknowledged that the intrinsic electronic conductivities of LFP and LATP are both very low (at room temperature: $\approx 10^{-6}$ mS cm^{-1}).[56,57] Nevertheless, the measured Nyquist plot shows no blocking tails, suggesting no blockage for electron transport. Therefore, the co-fired LFP/LATP composite cathode can be regarded as a mixed ionic and electronic conductor, which is required for the operation of ASSBs.

As shown in Figure 3a, the Nyquist plot of the co-fired LFP/LATP sample can be fitted using the inserted equivalent circuit.[58] The circuit has two parallel R/CPE combinations corresponding to the two semicircles on the Nyquist plot. The high- and low-frequency semicircles reflect the parallel combination of ionic response (R_i/CPE_i) and electronic response (R_e/CPE_{geo}), respectively. The intercept of the low-frequency semicircle with x-axis at the lowest frequency represents the electronic shunt resistance R_e due to the ionic transport pathway can be regarded as open as a result of the extremely high ionic impedance at low frequencies. Due to the system complexity, the separation of the bulk, homogeneous grain boundary and heterogeneous grain boundary (LFP/LFTAP, LFP/LATP, and LFTAP/LATP) ionic contributions is challenging even when the ultra-high frequency EIS (up to 3 GHz) was used for the measurement. Therefore, the R_i/CPE_i combination with the capacitance of 1.6×10^{-10} F (C_i) stands for the total ionic transport of the system. The sample/electrode interfacial capacitance of 1.2×10^{-7} F (C_{int}) and the sample geometric capacitance of 6.5×10^{-12} F (C_{geom}) are in agreement with literature values, demonstrating the feasibility of this assignment.[58,59]

Based on the obtained ionic resistance (126.9 Ω) and electronic resistance (17.1 Ω), the σ_i and σ_e of the co-fired LFP/LATP are calculated to be 0.99 and 7.41 mS cm^{-1} at 60 °C, respectively. These are sufficiently high for battery operation at 60 °C due to the much higher σ_e than σ_i when considering each de-/intercalation only need a pair of Li-ion and electron. It is worth noting that the grain boundary resistances in NASICON-type compounds are usually ≈10 times higher than that of the bulk, implying the grain boundary resistance mainly determines the total ionic conductivity of the co-fired LFP/LATP.[34,60,61] As the LFP/LATP interface is modified by a thick layer (40–100 nm) of LFTAP interphase, the ionically conductive nature of LFTAP is the determining factor for the sample to achieve the high σ_i. The σ_e of the sample was further verified to be 7.28 mS cm^{-1} at 60 °C by DC measurement, which is consistent with the EIS result (Figure S9a, Supporting Information). Such high electronic conductivity originates from continuous electron pathways around LATP and LFP particles, synergistically constructed by the remaining carbon on LFP surfaces and the LFTAP interphase. The electronic conductivity of the complex LFTAP phase, one of the "polyanion" compounds, is promoted by the high valence cation non-stoichiometry doping effect.[62] Moreover, as a consequence of carbon oxidation and loss during co-firing, Ti^{4+} may partially reduce to Ti^{3+} to form multivalent LFTAP composite interphase, which could increase the concentration of electron carriers and further enhance the σ_e of the sample.[63]

Based on the obtained σ_i and σ_e at different measured temperatures, the activation energies of ionic and electronic conductivities (E_a(Li) and E_a(e), respectively) are calculated to be 0.29 and 0.07 eV, respectively (Figure 3b; Figure S9b, Supporting Information). The E_a(Li) of the co-fired LFP/LATP sample is in agreement with the reported total ionic activation energies of LATP.[34,64,65] The obtained E_a(Li) is much lower than that of the lowest theoretical energy barrier of 0.60 eV in pure LFP,[66] suggesting that the ion transport inside the composite cathode is mainly through the NASICON-type LATP and LFTAP phases. Besides, attributed to the shortened electronic diffusion path in the dense co-fired LFP/LATP composite cathode, a low E_a(e) of 0.07 eV is achieved.

To further demonstrate the improved Li^+ and e^- transport capabilities, the electrical properties of the co-fired LFP/LATP are compared with those of the cold-pressed LFP/LATP (room temperature isostatic pressed at 500 MPa for 30 s). It is evidenced from Figure 3c that the ionic and electronic conductivities of the co-fired LFP/LATP are about three orders of magnitudes higher than those of the cold-pressed LFP/LATP (Nyquist and Arrhenius plots for the cold-pressed LFP/LATP are shown in Figure S9c and S9d, respectively, Supporting Information). Besides, the E_a(Li) and E_a(e) of the co-fired LFP/LATP are much lower than those of the cold-pressed LFP/LATP. Graphical images of physical contact for cold-pressed LFP/LATP and sintering contact for co-fired LFP/LATP are comparatively explained to understand the underlying reasons for the significantly enhanced Li^+ and e^- mobilities by co-firing (Figure 3d). The cold-pressed LFP/LATP is highly porous (relative density: ≈60%) with weak mechanical strength and physical point contacts between LFP/LATP particles. The interfacial area between the cold-pressed LFP/LATP is extremely limited due to rather poor contacts. Consequently, Li^+ can only migrate through very narrow interfaces made by point contacts, resulting in a high tortuosity for both ionic and electronic conductions. In contrast, LFP and LATP composite cathode is able to be densified into high relative density around 90% after co-firing at 775 °C. The compact structure is beneficial for shortening the diffusion pathways for both ions and electrons. Moreover, in the present case, elemental inter-diffusion at the high sintering temperature promotes the formation of conductive LFTAP interphase, which not only enhances the mechanical strength of the composite cathode by establishing firm sintering bridges between LFP/LATP particles but also facilitates fast Li^+/e^- transportations at the LFP/LATP interface.[67]

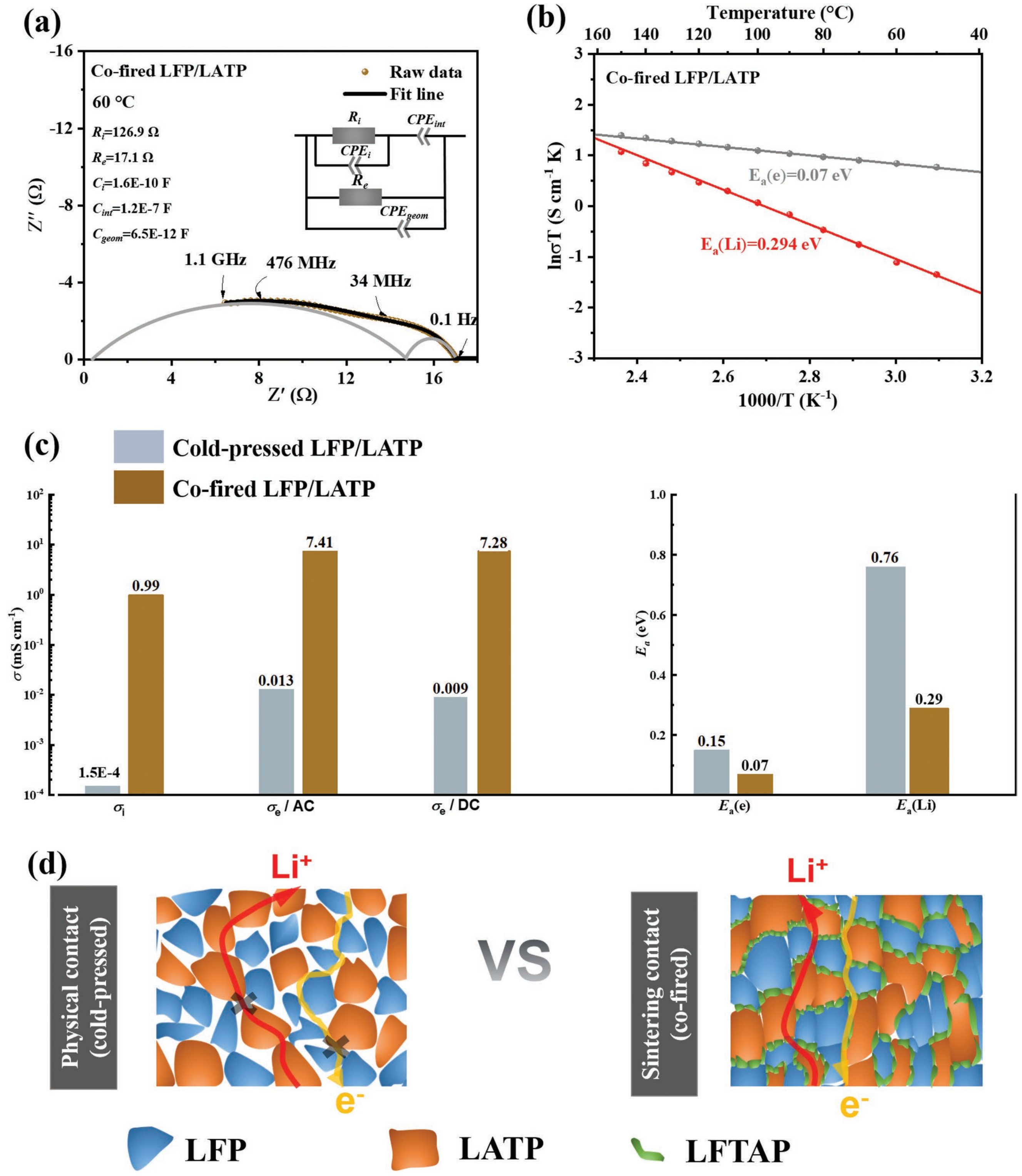

Figure 3. a) The fitted Nyquist plot of the co-fired LFP/LATP pellet measured at 60 °C with inserted equivalent circuit model b) Arrhenius plots for the ionic (E_a(Li)) and electronic (E_a(e)) conductions, respectively. c) Comparison of electrical properties of the cold-pressed LFP/LATP and co-fired LFP/LATP (60 °C). d) Schematic illustration of a cold-pressed LFP/LATP composite cathode and a co-fired LFP/LATP composite cathode and their respective transportation of ions and electrons. Sample size description, thickness (*L*): 0.88 mm, diameter (*d*): 9.45 mm for the co-fired LFP/LATP, and *L*: 0.92 mm, *d*: 10.15 mm for the cold-pressed LFP/LATP.

2.2. Electrochemical Performance of Co-Fired LFP/LATP Composite Cathode in ASSB

To study the electrochemical performance of the co-fired LFP/LATP composite cathode, ASSBs consisting of the co-fired LFP/LATP composite cathodes, modified salt in polymer $P(EO)_{15}LiTFSI$ solid electrolytes and Li metal anodes were fabricated and tested. Detailed properties of the used polymer electrolytes are discussed in the supporting information. Principally, the co-fired LFP/LATP composite cathode contains three electrochemically active components of LFP, LFTAP and LATP. LFP is a well-known CAM that undergoes two-phase electrochemical reactions accompanied by flat charge/discharge voltage plateaus (Fe^{2+}/Fe^{3+}) at around 3.5 V versus Li/Li^+.[68] Previous studies have reported the redox reactions of Fe^{2+}/Fe^{3+} and Ti^{3+}/Ti^{4+} in $Li_{1+x}Fe_xTi_{2-x}(PO_4)_3$ NASICON-type frameworks take place at around 2.7 and 2.4 V versus Li/Li^+, respectively.[35,69] Meanwhile, Li insertion/extraction in LATP is observed by Amiki et al. using cyclic voltammetry measurement in a Pt|LATP half-cell.[70] They showed the redox reaction of Ti^{3+}/Ti^{4+} in LATP occurs at around 2.4 V versus Li/Li^+, which is comparable with that of Ti^{3+}/Ti^{4+} in $Li_{1+x}Fe_xTi_{2-x}(PO_4)_3$ and $LiTi_2(PO_4)_3$.[35,38,69,70] Therefore, the cells were cycled under a constant current density of 36 μA cm^{-2} at 60 °C in three different voltage ranges of 4.1–2.8 V, 4.1–2.5 V, and 4.1–2.2 V to study the electrochemical behavior of the co-fired LFP/LATP composite cathode. The evolution of cell polarizations was monitored by EIS measurements.

Figure 4a, c, e presents the charge–discharge profiles for the first ten cycles of the cells discharged down to 2.8, 2.5, and 2.2 V, respectively. For the cell with discharge cut-off voltage at 2.8 V, the charge- and discharge-plateaus are found at ≈3.5 and ≈3.3 V, respectively, corresponding to the redox process of $LiFePO_4 \leftrightarrow FePO_4$ (LFP ↔ FP, I′/I). For the cell with discharge cut-off voltage at 2.5 V, the charge-discharge profiles contain two redox processes. In addition to the redox-reaction of LFP ↔ FP at 3.5/3.3 V (I′/I), another oxidation/reduction process at 2.9 V/2.7 V (II′/II) is observed, which is consistent with the Li^+ de-intercalation/intercalation voltages of Fe^{3+}/Fe^{2+} in LFTAP.[35] For the cell with discharge cut-off voltage at 2.2 V, the third pair of charge/discharge-plateaus belonging to the redox-reaction of Ti^{4+}/Ti^{3+} in LFTAP and LATP at 2.5 V/2.3 V (III′/III) is discovered. These verify that all the constituting components (LFP, LFTAP, and LATP) in the co-fired LFP/LATP composite cathode are electrochemically active.

The capacities of the cells with discharge cut-off voltage at 2.8 and 2.5 V continuously increased with the increasing cycling numbers (Figure 4a,c). Firstly, by comparing the Nyquist plots of the fresh and cycled cells, it is found that the total cell resistances are reduced upon cycling for both cells until reaching relatively steady states at the 7th cycle with a minimum total cell resistance ≈300 Ω (Figure 4b,d). The decline of total cell resistance is mainly attributed to the enhanced Li^+ transport capabilities within the MSPE and the contact improvement of the composite cathode/MSPE and MSPE/Li interfaces (see Figures S11,S12, Supporting Information, and the following discussion in the Supporting Information for more detail). Such effects are reflected by the reducing slopes of charge/discharge curves for LFP. Secondly, the co-fired LFP/LATP composite cathode could have poor diffusion properties of Li-ions and electrons within the large grain-sized LFP (≈1 μm) and LFP primary particle agglomerates (Figure S4, Supporting Information).[71,72] The low Li^+/e^- kinetic in the bulk LFP leads to high concentration polarization, representing by the sloped discharge profiles approaching the end of discharge for LFP (Figure 4a,c). Consequently, the inner-cores of some large LFP particles are electrochemically inaccessible, resulting in a low capacity in the first few cycles. Nevertheless, it seems LFP in the co-fired LFP/LATP composite cathode could be activated by charge–discharge because taking out of Li-ions allows higher transportations of both ions and electrons within LFP.[73,74] Therefore, more active sites are available for the next charge-discharge cycle until a steady state is reached. The cell with discharge cut-off voltage at 2.2 V has the same trend of increasing capacity until the 4th cycle (Figure 4e,f). Then, the capacity slightly reduces and maintains almost constant from the 7th to 10th cycle.

In the 10th cycle, cells with discharge cut-off voltage at 2.8, 2.5, and 2.2 V can achieve specific discharge capacities of 150.7, 170.1, and 245.6 mAh g^{-1}, respectively. Here, the specific capacities of the cells are calculated based on the mass loadings of LFP. For the cells with discharge cut-off voltage at 2.8 V, only Fe^{2+}/Fe^{3+} redox reaction in LFP takes place that the discharge capacity obtained solely comes from LFP (Figure 4a). For the cells with lower discharge cut-off voltages (2.5 and 2.2 V), higher discharge capacities are reached which are mainly attributed to LFTAP and LATP in the composite cathode are involved in the redox processes, contributing additional capacities (Figure 4c,e). It is important to mention that the evaluation of LFTAP capacity contribution is challenging because the LFTAP discharge plateaus are assumed to be influenced by the lithiation process of FP due to the concentration polarization. Nevertheless, the overall utilization of the loaded LFP and LATP can be calculated for the cell with discharge cut-off voltage at 2.2 V. Based on the areal loading of LFP (11.5 mg cm^{-2}) and LATP (9.7 mg cm^{-2}) in the composite cathode as well as their respective theoretical capacities (LFP: 170 mAh g^{-1} and LATP: 119 mAh g^{-1}), 90.3% of the theoretical capacity of the loaded materials are delivered that the cell can achieve a high discharge areal capacity of 2.8 mAh cm^{-2} after the 10th cycle. This suggests that the LFTAP and LATP in co-fired composite cathode have good Li^+ de-intercalation/intercalation properties. Also, the LFTAP interphase is quite stable regarding activating all components in the co-fired LFP/LATP composite cathode.

Additionally, rate capability and long term cycling performance of the cells with discharge cut-off voltage at 2.8 and 2.5 V were evaluated to elucidate the interphase stability of the co-fired LFP/LATP composite cathode. After ten charge–discharge cycles at a current density of 36 μA cm^{-2}, the cells were cycled at higher current densities up to 144 μA cm^{-2} and then returned to 36 μA cm^{-2} (Figure S13a,b, Supporting Information). The specific discharge capacities for the cells with discharge cut-off voltage at 2.8 and 2.5 V are found to be 151, 96, 64, 45 mAh g^{-1} and 170, 123, 83, 57 mAh g^{-1}, respectively, at cycling current density of 36, 72, 108, 144 μA cm^{-2} (Figure S13c,d, Supporting Information). With increasing the current density, the discharge capacities decrease, the overpotentials and concentration polarizations increase for both cells, implying the rate performance

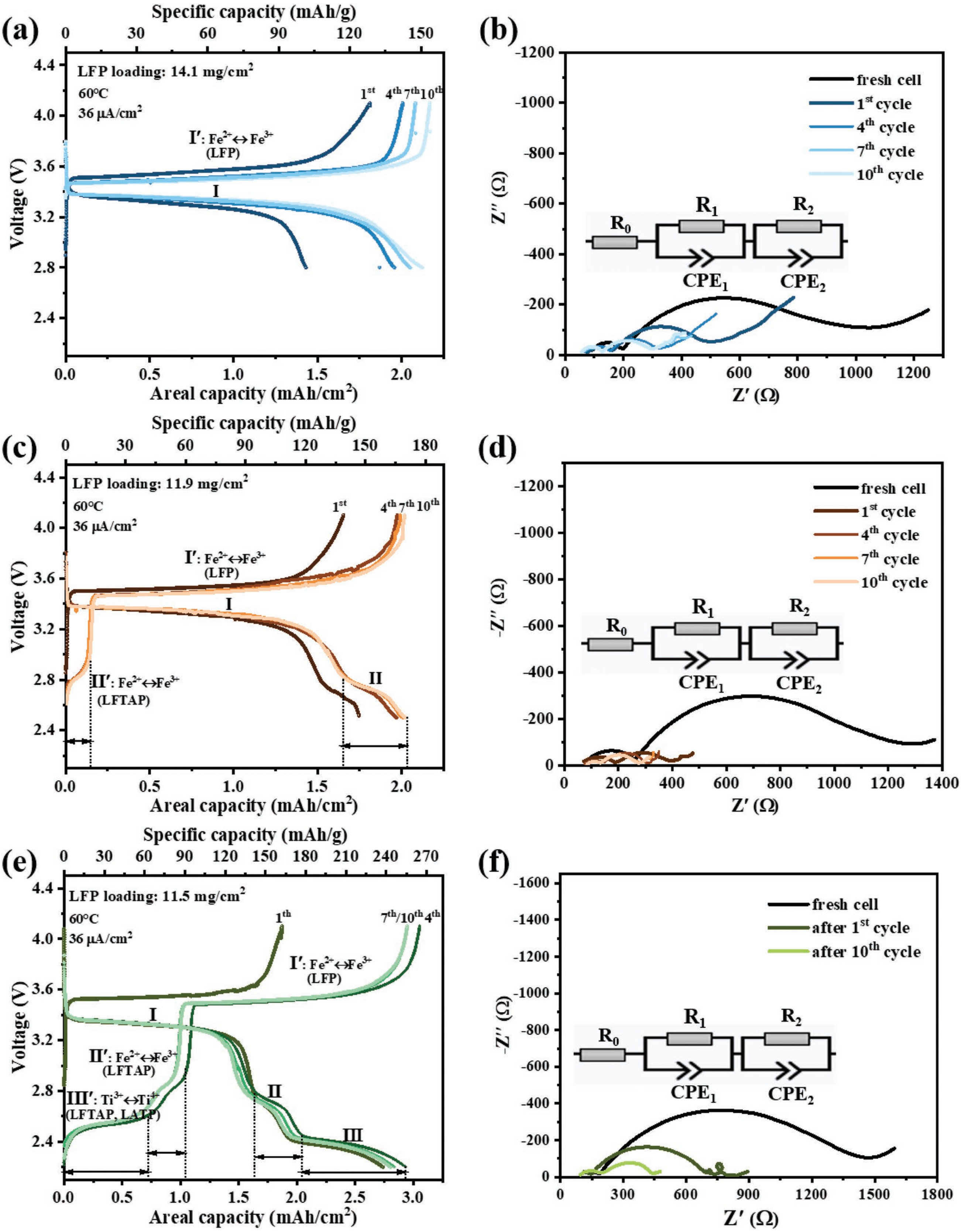

Figure 4. Galvanostatic charge and discharge profiles of cells cycled in the voltage range of a) 4.1–2.8 V, c) 4.1–2.5 V, and e) 4.1–2.2 V (cycle number 1, 4, 7, 10 charge/discharge profiles are shown for each cell, specific capacity is calculated based on the mass loading of LFP). Nyquist plots and inserted equivalent circuits of the fresh cells and cycled cells in the voltage range of b) 4.1–2.8 V, d) 4.1–2.5 V, and f) 4.1–2.2 V.

of the ASSBs is limited by the Li^+ transport kinetic in the MSPE and the composite cathode. Nevertheless, the discharge capacities can be fully recovered to the initial values when the current density is decreased to 36 µA cm^{-2} for both cells, demonstrating that the interphase of the composite cathode is stable at high current densities regardless of being activated or not.

Interestingly, it is found that the charge plateaus of $Fe^{2+} \leftrightarrow Fe^{3+}$ in LFTAP (II′) and $Ti^{3+} \leftrightarrow Ti^{4+}$ in LFTAP/LATP (III′) are shorter than their respective discharge plateaus (II and III) (Figure 4c,e). In the meanwhile, the cells display substantially larger charge plateaus of $Fe^{2+} \leftrightarrow Fe^{3+}$ in LFP than their discharge plateaus. To study this asymmetric charge-discharge behavior, asymmetric charge-discharge measurements of the cell cycled in the voltage range of 4.1–2.5 V were performed after ten constant current charge-discharge cycles at 36 µA cm^{-2}. As presented in **Figure 5**a, when the cell is charged at a constant current density of 36 µA cm^{-2} and discharged with increasing current densities from 36 to 144 µA cm^{-2}, the discharge capacity of the cell reduces quickly from 165 mAh g^{-1} at 36 µA cm^{-2} to 45 mAh g^{-1} at 144 µA cm^{-2}. In contrast, when the cell is charged with increasing current densities from 36 to 144 µA cm^{-2} and discharged at a constant density of 36 µA cm^{-2}, the discharge capacity of each cycle is only slightly reduced from 165 mAh g^{-1} at 36 µA cm^{-2} to 125 mAh g^{-1} at 144 µA cm^{-2} (Figure 5b). Besides, it is worth noting that the discharge plateaus of $Fe^{2+} \leftrightarrow Fe^{3+}$ in LFTAP are present regardless of changing charge/discharge current densities. However, their respective charge plateaus are substantially shorter or even disappeared under higher discharge current densities (≥72 µA cm^{-2}). These imply that the discharge process is more sluggish than that of charge, which might lead to partial Li-ions transiently intercalating into the LFTAP lattice and gradually diffusing to FP to reach a higher lithiation degree during discharge.

To further analyze the Li^+ transport properties in the co-fired LFP/LATP composite cathode at different charged/discharged states, EIS measurements of the cell with discharge cut-off voltage at 2.2 V were carried out at various states of charge (Figure 5c). Figure 5d lists the total resistances of the cell at seven different charged/discharged states in the 11th cycle obtained from the measured Nyquist plots (Figure S14, Supporting Information). The total resistances of the cell obtained at the end of discharge for the 10th (point 0) and 11th (point 6)

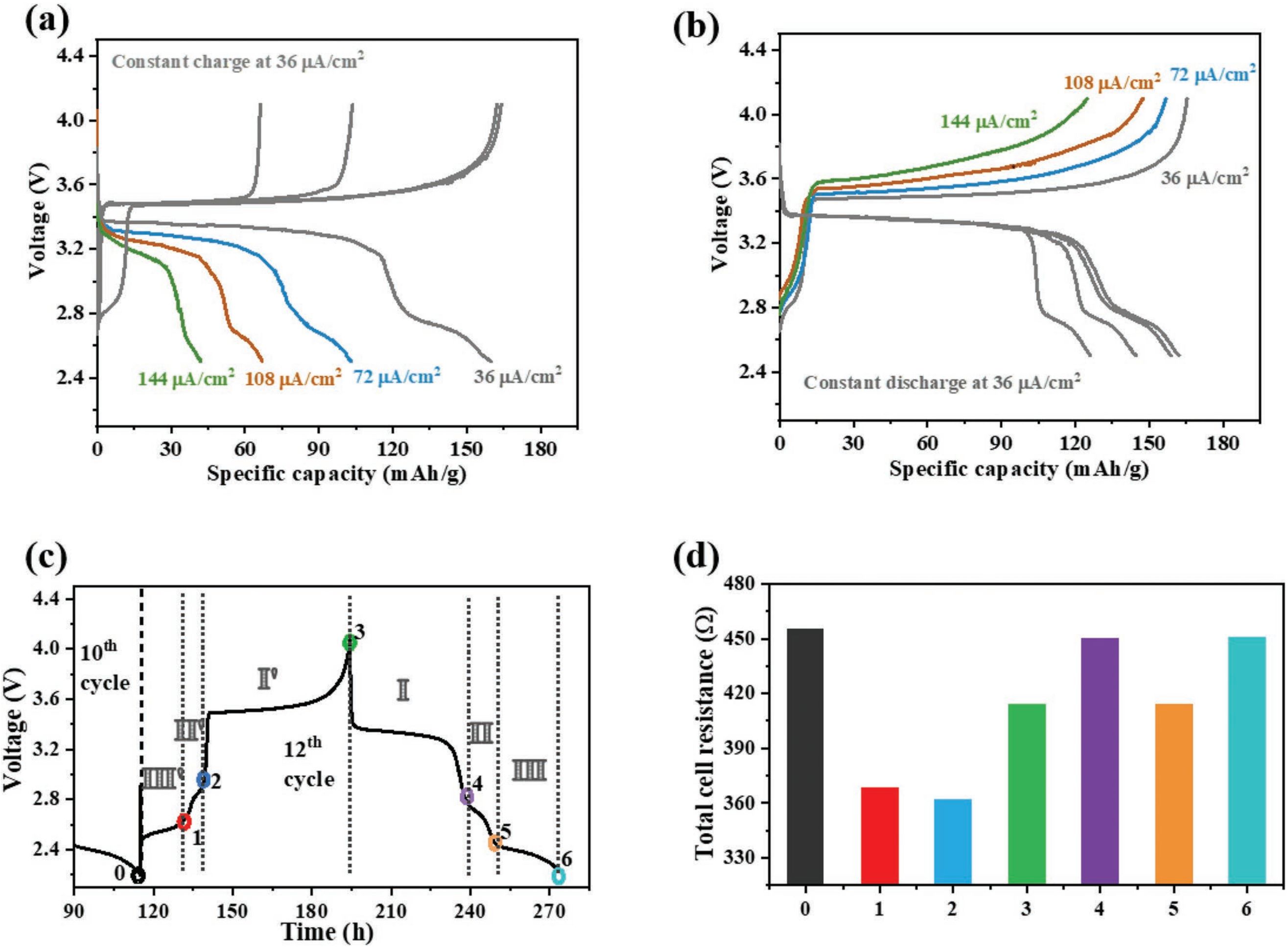

Figure 5. Asymmetric charge-discharge profiles measured at 60 °C of the cell cycled in the voltage range of 4.1–2.5 V; a) the cell is charged at a constant current density of 36 µA cm^{-2} and discharged at increasing current densities; b) the cell is charged at increasing current densities and discharged at 36 µA cm^{-2}. c) Galvanostatic charge–discharge profiles along time and the corresponding d) total resistance of the cell cycled in the voltage range 4.1–2.2 V at various states of charge/discharge referring to points indicated in (c).

cycles are consistent with each other, demonstrating the cell is in a constant state after each discharge. This also suggests that the resistance of MSPE maintains steady during the charge–discharge process and the interfacial contacts between MSPE/composite cathode and MSPE/Li have reached optimum conditions. The change of total cell resistance is mainly ascribed to the different Li^+ transport kinetic originating from the co-fired LFP/LATP composite cathode at various charged/discharged states.

At the beginning of charge and end of discharge (cf. points 0 and 6, respectively), LFP, LFTAP and LATP are in "completely" lithiated states and the cell exhibits the highest resistance. This is attributed to the sluggish Li^+ diffusion because of the reduced number of free Li^+ vacancy/interstitial sites at the fully charged state.[75,76] Experimentally, it is also discovered that the total resistance of the cell that discharged to 2.2 V after ten cycles (≈450 Ω) is higher than those of the cells with discharge cut-off voltages at 2.8 and 2.5 V (≈300 Ω) (Figure 4b,d,f). As delithiation proceeds, the freeing up of partial Li^+ sites in LFTAP and LATP may positively affect the Li^+ transport kinetic. Thus, at point 1 (2.6 V) and point 2 (3.0 V), the composite cathode with delithiated LFTAP and LATP have smaller resistances than those of point 0/6 (2.2 V). Point 3 (4.1 V) has slightly higher resistance compared with that of point 1 (2.6 V) and point 2 (3.0 V). The reason could be that the deeply charged electrodes may have a lower Li^+ diffusion coefficient due to the non-sufficient Li^+ available.[77,78] Besides, attributed to the increased electrochemical potential of FP at the end of charging, a resistive space charge layer between FP and LFTAP could be formed as a result of their Li^+ concentration difference.[79] During discharge, unexpectedly, the total resistance of the composite cathode at point 4 (2.8 V) is considerably higher than that of point 2 (3.0 V) despite principally they should have the same lithiation states of LFP, LFTAP, and LATP. The similar phenomenon is observed when comparing the resistance at point 5 (2.5 V) and point 1 (2.6 V). These suggest that Li-ions transport under higher resistance in discharge than that of charge, aligning with the observed phenomena of different charge/discharge responses for the cell cycled between 4.1 and 2.5 V to the increased current densities (Figure 5a,b).

As illustrated in **Figure 6**, a schematically drawing is employed to understand the phenomena of asymmetric total cell resistance upon charging and discharging processes. Since the major part of composite cathode resistance originates from the charge transfer resistances through the heterogeneous interfaces, the evolution of LFP/LFTAP and LFTAP/LATP interfacial barriers upon Li^+ uptake/extraction is depicted graphically. In general, the interfacial barrier between LFP and LFTAP is higher than that between LFTAP and LATP because the NASICON-LFTAP interphase has crystallographic heterogeneity with olivine-LFP and homogeneity with NASICON-LATP.[2,80]

It can be seen in Figure 6 that during stage III′ and II′ in charge, the processes of Li^+ de-intercalated first from LFTAP and LATP, and then from LFTAP are rather fast and smooth due to the highly ionic conductive NASICON-type LFTAP/LATP and the small LFTAP/LATP interfacial barrier. With increasing the depth of charge, despite a higher LFP/LFTAP interfacial barrier, the delithiation process of LFP (I′) could proceed consistently and continuously because the Li^+ flux is always moving to more ionic conductive components. When it comes to the discharging process, the transportation of Li^+ flux through LATP→LFTAP→LFP enables the lithiation of FP (I). However, the fast movement of Li^+ flux from LATP to LFTAP and the slow movement from LFTAP to LFP introduce a rate mismatch in the charge transfer direction. Besides, the phase transformation from FP to LFP is more sluggish than that from LFP to FP, especially at higher current rates.[81,82] According to the widely accepted "shrinking-core" model of LFP, a resistive LFP shell is formed with a continuous shrinking of the FP core upon discharge.[83] In our ASSB system, although the co-fired LFP/LATP composite cathode is operated at a relatively low current density, the micro-sized LFP grain could still suffer from insufficient Li^+ diffusion through the progressively thicker LFP shell. Therefore, high concentration polarization and obvious voltage drop during discharge are observed. When the discharge voltage meets the reduction potential of the Fe^{3+} in LFTAP interphase, instead of lithiating FP, Li-ions favor to occupy the Li^+ sites in LFTAP with shorter diffusion length. Consequently, a Li^+ enriched zone is formed in the interfacial region between LFP/LFTAP, impeding Li^+ transport kinetic at the end of stage I. Meanwhile, on account of the high electrochemical potential of the unlithiated FP, some Li-ions are forced to move from the Li^+ enriched LFTAP interphase to LFP during stage II, enabling a slight reduction of the LFP/LFTAP interfacial resistance and allowing gradual movement of Li-ions to FP to reach a higher lithiation degree.[84] While LFP is approaching the fully discharged state, Li-ions start to stably occupy available Li^+ sites throughout bulk LFTAP and LATP during stage II and III.

The hypothesis of transient Li^+ intercalation into LFTAP is in accordance with the experimental observation. For the cells with discharge cut-off voltages at 2.5 and 2.2 V, the discharge plateaus (II and III) are more extended compared with the charge plateaus (II′ and III′) (Figure 4c,e). Moreover, the hypothesis mutually corroborates with the diminished charging plateaus of LFTAP for the cell cycled between 4.1 and 2.5 V with increasing discharge current densities (Figure 5a). Based on these, it can be concluded that the active LFTAP interphase acts as a "double-edged sword," which could lead to a higher composite cathode resistance during discharge than that of charge and, on the other hand, serve as a temporarily "reservoir" to store Li-ions, mitigating the inferior Li^+ transport kinetic within bulk LFP and allowing Li^+ diffusion spontaneously into FP in a longer time spatial.

3. Conclusion

In summary, a robust and densified composite cathode was prepared by co-firing a homogeneous mixture of LFP active material powders and LATP electrolyte powders. After co-firing, a crystallized NASICON-type LFTAP interphase formed between LFP and LATP particles. Attributed to the compacted structure and ionic conductive LFTAP interphase, the co-fired LFP/LATP composite cathode possesses competitive ionic and electronic conductivities of 0.99 and 7.41 mS cm^{-1} at 60 °C, respectively. ASSBs composed of the co-fired LFP/LATP composite cathodes, solid polymer electrolytes and Li metal anodes were stably

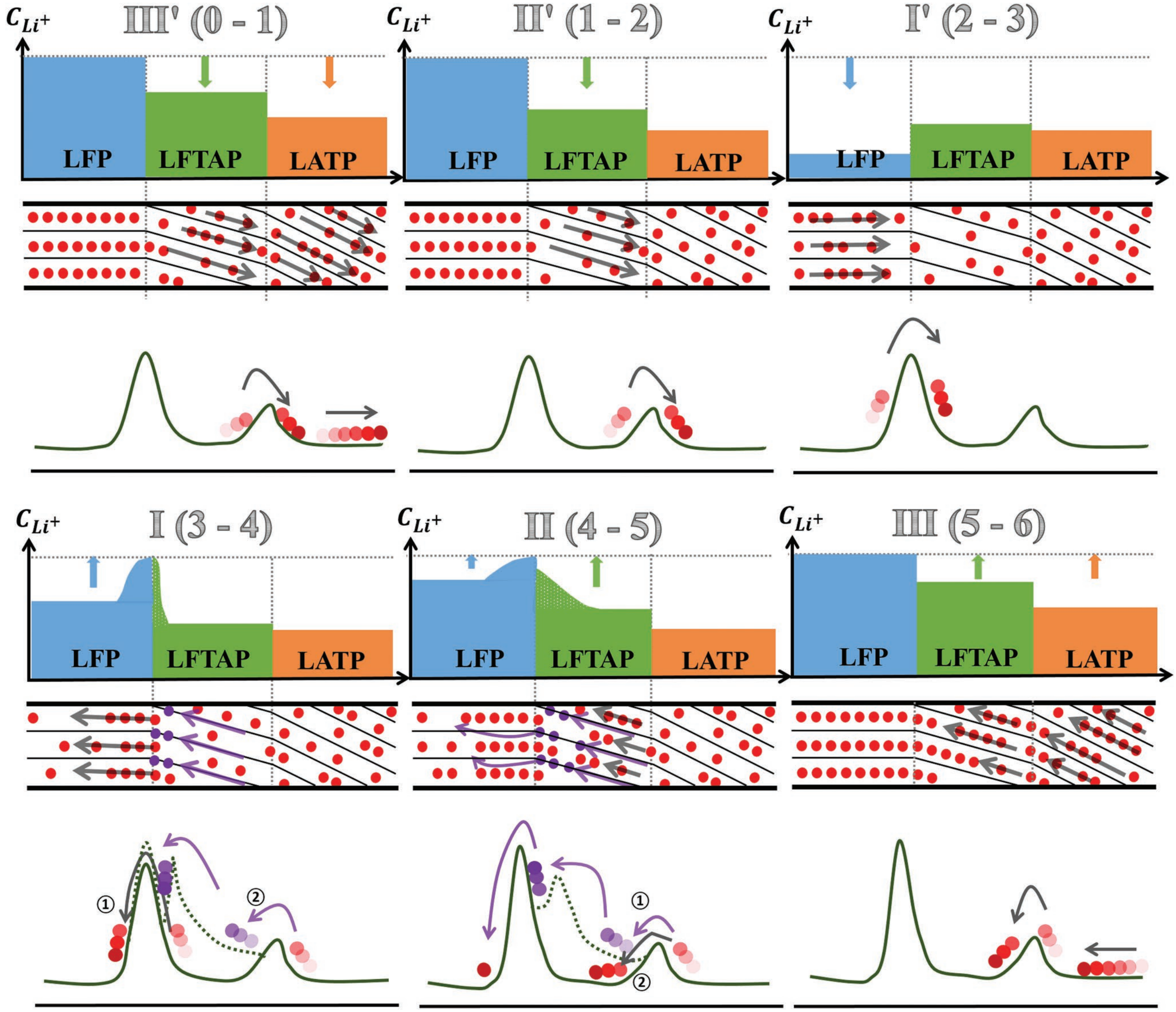

Figure 6. Illustration and comparison of the charge/discharge stages of the co-fired LFP/LATP composite cathode in the voltage range of 4.1–2.2 V with schematically depicted normalized Li^+ concentration (C_{Li^+}) in LFP (blue), LFTAP (green), and LATP (orange), Li^+ occupancy sites (red and purple solid circles represent stably and transiently occupied Li^+ sites in LFTAP, respectively) and interfacial barrier profiles for Li^+ transportation (the different charge/discharge stages of I′/I, II′/II, and III′/III are corresponding to the galvanostatic charge–discharge profiles in Figure 5c).

cycled in three different voltage ranges of 4.1–2.8, 4.1–2.5, and 4.1–2.2 V. Attributed to the high structural stability of the co-fired LFP/LATP composite cathode, extra reversible capacity could be delivered from the redox reactions of the formed LFTAP interphase and LATP by lowering the discharge cut-off voltage to 2.5 and 2.2 V, respectively. In addition, the asymmetric charge-discharge profiles of the ASSBs by activating the LFTAP interphase reveal that the Li^+ kinetic in the co-fired LFP/LATP composite cathode depends strongly on the direction of phase transformation. The charge process is smooth and barrier-less with reduced composite cathode resistance by freeing up the Li^+ sites in the LFTAP interphase. In contrast, the discharge process is sluggish because of the enrichment of Li^+ in the LFP/LFTAP interfacial region due to the redox-active nature of the LFTAP interphase. This work highlights the effects of the electrochemically active interphase on the electrochemical behavior of all-phosphate based composite cathode and provides insights for interphase design in the composite cathode to build bulk-type ASSBs with stable battery performance and industry relevant areal capacities. The co-firing method can be potentially applied to high voltage phosphate cathodes such as $LiMnPO_4$, $LiCoPO_4$, or $LiNiPO_4$, owing to their similar crystallization temperatures and the same crystallographic structure compared with those of LFP. Thus, energy and power densities of the relevant ASSBs could be further improved.

4. Experimental Section

See the Supporting Information.

Supporting Information

Supporting Information is available from the Wiley Online Library or from the author.

Acknowledgements

This work was financially supported by the project of "Materials and Components to Meet High Energy Density Batteries III" of the funding program "Excellent battery" from the Bundesministerium für Bildung und Forschung (BMBF) (Project No.: 13XP0258B), and the project "High Performance Solid-State Batteries" (HIPSTER) from "Ministerium für Kultur und Wissenschaft des Landes Nordrhein-Westfalen."

Open access funding enabled and organized by Projekt DEAL.

Conflict of Interest

The authors declare no conflict of interest.

Author Contributions

All authors made contributions to manuscript preparation and have given final approval for publication.

Data Availability Statement

The data that support the findings of this study are available from the corresponding author upon reasonable request.

Keywords

active interphases, co-fired LFP/LATP composite cathodes, high areal capacity, LATP redox

Received: January 13, 2022
Revised: April 5, 2022
Published online: April 27, 2022

---

[1] C. P. Grey, D. S. Hall, *Nat. Commun.* **2020**, *11*, 6279.
[2] C. Chen, M. Jiang, T. Zhou, L. Raijmakers, E. Vezhlev, B. Wu, T. U. Schülli, D. L. Danilov, Y. Wei, R. A. Eichel, P. H. L. Notten, *Adv. Energy Mater.* **2021**, *11*, 2003939.
[3] C. Yu, S. Ganapathy, E. R. H. V. Eck, H. Wang, S. Basak, Z. Li, M. Wagemaker, *Nat. Commun.* **2017**, *8*, 1086.
[4] Y. Xiao, L. J. Miara, Y. Wang, G. Ceder, *Joule* **2019**, *3*, 1252.
[5] Y. Li, D. Zhang, X. Xu, Z. Wang, Z. Liu, J. Shen, J. Liu, M. Zhu, *J. Energy Chem.* **2021**, *60*, 32.
[6] A. Banerjee, X. Wang, C. Fang, E. A. Wu, Y. S. Meng, *Chem. Rev.* **2020**, *120*, 6878.
[7] S. Wang, H. Xu, W. Li, A. Dolocan, A. Manthiram, *J. Am. Chem. Soc.* **2018**, *140*, 250.
[8] F. Han, J. Yue, C. Chen, N. Zhao, X. Fan, Z. Ma, T. Gao, F. Wang, X. Guo, C. Wang, *Joule* **2018**, *2*, 497.
[9] X. Ren, X. Zhang, Z. Shadike, L. Zou, H. Jia, X. Cao, M. H. Engelhard, B. E. Matthews, C. Wang, B. W. Arey, X. Q. Yang, J. Liu, J. G. Zhang, W. Xu, *Adv. Mater.* **2020**, *32*, 2004898.
[10] M. Du, K. Liao, Q. Lu, Z. Shao, *Energy Environ. Sci.* **2019**, *12*, 1780.
[11] D. Zhang, X. Xu, X. Huang, Z. Shi, Z. Wang, Z. Liu, R. Hu, J. Liu, M. Zhu, *J. Mater. Chem. A* **2020**, *8*, 18043.
[12] R. Li, K. Liao, W. Zhou, X. Li, D. Meng, R. Cai, Z. Shao, *J. Membr. Sci.* **2019**, *582*, 194.
[13] A. Sakuda, H. Kitaura, A. Hayashi, K. Tadanaga, M. Tatsumisago, *J. Power Sources* **2009**, *189*, 527.
[14] F. Strauss, J. H. Teo, J. Maibach, A. Y. Kim, A. Mazilkin, J. Janek, T. Brezesinski, *ACS Appl. Mater. Interfaces* **2020**, *12*, 57146.
[15] C. Wang, J. Liang, S. Hwang, X. Li, Y. Zhao, K. Adair, C. Zhao, X. Li, S. Deng, X. Lin, X. Yang, R. Li, H. Huang, L. Zhang, S. Lu, D. Su, X. Sun, *Nano Energy* **2020**, *72*, 104686.
[16] Y. Zhu, X. He, Y. Mo, *J. Mater. Chem. A* **2016**, *4*, 3253.
[17] T. Yoshinari, R. Koerver, P. Hofmann, Y. Uchimoto, W. G. Zeier, J. Janek, *ACS Appl. Mater. Interfaces* **2019**, *11*, 23244.
[18] D. Zhang, X. Xu, Y. Qin, S. Ji, Y. Huo, Z. Wang, Z. Liu, J. Shen, J. Liu, *Chem. – Eur. J.* **2020**, *26*, 1720.
[19] O. Levit, P. Xu, B. Shvartsev, G. Avioz Cohen, L. Stanciu, Y. Tsur, Y. Ein-Eli, *Energy Technol.* **2020**, *8*, 2000634.
[20] M. Du, Y. Sun, B. Liu, B. Chen, K. Liao, R. Ran, R. Cai, W. Zhou, Z. Shao, *Adv. Funct. Mater.* **2021**, *31*, 2101556.
[21] N. Zhang, X. Long, Z. Wang, P. Yu, F. Han, J. Fu, G. Ren, Y. Wu, S. Zheng, W. Huang, C. Wang, H. Li, X. Liu, *ACS Appl. Energy Mater.* **2018**, *1*, 5968.
[22] L. Miara, A. Windmüller, C. L. Tsai, W. D. Richards, Q. Ma, S. Uhlenbruck, O. Guillon, G. Ceder, *ACS Appl. Mater. Interfaces* **2016**, *8*, 26842.
[23] M. Kotobuki, Y. Suzuki, H. Munakata, K. Kanamura, Y. Sato, K. Yamamoto, T. Yoshida, *J. Power Sources* **2010**, *195*, 5784.
[24] K. J. Kim, J. L. M. Rupp, *Energy Environ. Sci.* **2020**, *13*, 4930.
[25] J. P. Beaupain, K. Waetzig, S. Otto, A. Henss, J. Janek, M. Malaki, A. Pokle, J. Mu, B. Butz, K. Volz, M. Kusnezo, A. Michaelis, *ACS Appl. Mater. Interfaces* **2021**, *13*, 47488.
[26] Q. Ma, Q. Xu, C.-L. Tsai, F. Tietz, O. Guillon, *J. Am. Ceram. Soc.* **2015**, *99*, 410.
[27] S. D. Jackman, R. A. Cutler, *J. Power Sources* **2013**, *230*, 251.
[28] G. Yan, S. Yu, J. F. Nonemacher, H. Tempel, H. Kungl, J. Malzbender, R. A. Eichel, M. Krüger, *Ceram. Int.* **2019**, *45*, 14697.
[29] A. Manthiram, *Nat. Commun.* **2020**, *11*, 1550.
[30] M. Gellert, E. Dashjav, D. Grüner, Q. Ma, F. Tietz, *Ionics (Kiel)* **2018**, *24*, 1001.
[31] M. Sugantha, U. V. Varadaraju, *Solid State Ionics* **1997**, *95*, 201.
[32] A. Venkateswara Rao, V. Veeraiah, A. V. Prasada Rao, B. K. Babu, *Res. Chem. Intermed.* **2015**, *41*, 2307.
[33] R. DeWees, H. Wang, *ChemSusChem* **2019**, *12*, 3713.
[34] Q. Xu, C. L. Tsai, D. Song, S. Basak, H. Kungl, H. Tempel, F. Hausen, S. Yu, R. A. Eichel, *J. Power Sources* **2021**, *492*, 229631.
[35] S. Patoux, G. Rousse, J. B. Leriche, C. Masquelier, *Solid State Sci.* **2004**, *6*, 1113.
[36] G. X. Wang, D. H. Bradhurst, S. X. Dou, H. K. Liu, *J. Power Sources* **2003**, *124*, 231.
[37] V. A. Sugiawati, F. Vacandio, C. Perrin-Pellegrino, A. Galeyeva, A. P. Kurbatov, T. Djenizian, *Sci. Rep.* **2019**, *9*, 11172.
[38] S. Yu, A. Mertens, H. Tempel, R. Schierholz, H. Kungl, R. A. Eichel, *ACS Appl. Mater. Interfaces* **2018**, *10*, 22264.
[39] R. Amin, Y.-M. Chiang, *J. Electrochem. Soc.* **2016**, *163*, A1512.
[40] M. Park, X. Zhang, M. Chung, G. B. Less, A. M. Sastry, *J. Power Sources* **2010**, *195*, 7904.
[41] J. Auvergniot, A. Cassel, D. Foix, V. Viallet, V. Seznec, R. Dedryvère, *Solid State Ionics* **2017**, *300*, 78.
[42] T. Hakari, M. Deguchi, K. Mitsuhara, T. Ohta, K. Saito, Y. Orikasa, Y. Uchimoto, Y. Kowada, A. Hayashi, M. Tatsumisago, *Chem. Mater.* **2017**, *29*, 4768.
[43] R. Koerver, F. Walther, I. Aygün, J. Sann, C. Dietrich, W. G. Zeier, J. Janek, *J. Mater. Chem. A* **2017**, *5*, 22750.

[44] K. N. Wood, K. X. Steirer, S. E. Hafner, C. Ban, S. Santhanagopalan, S. H. Lee, G. Teeter, *Nat. Commun.* **2018**, *9*, 2490.
[45] N. Nitta, F. Wu, J. T. Lee, G. Yushin, *Mater. Today* **2015**, *18*, 252.
[46] N. Anantharamulu, K. Koteswara Rao, G. Rambabu, B. Vijaya Kumar, V. Radha, M. Vithal, *J. Mater. Sci.* **2011**, *46*, 2821.
[47] R. D. Shannon, *Acta Crystallogr., Sect. A: Found. Adv.* **1976**, *A32*, 751.
[48] S. Hamdoune, M. Gondrend, D. T. Qtti, *Mater. Res. Bull.* **1986**, *21*, 237.
[49] M. Catti, A. Comotti, S. Di Blas, R. M. Ibberson, *J. Mater. Chem.* **2004**, *14*, 835.
[50] J. P. Gross, J. Malzbender, E. Dashjav, F. Tietz, R. Schwaiger, *J. Mater. Sci.* **2022**, *57*, 925.
[51] V. A. Streltsov, E. L. Belokoneva, V. G. Tsirelson, N. K. Hansen, *Acta Crystallogr., Sect. B: Struct. Sci., Cryst. Eng. Mater.* **1993**, *49*, 147.
[52] K. Arbi, W. Bucheli, R. Jiménez, J. Sanz, *J. Eur. Ceram. Soc.* **2015**, *35*, 1477.
[53] J. Cabana, J. Shirakawa, G. Chen, T. J. Richardson, C. P. Grey, *Chem. Mater.* **2010**, *22*, 1249.
[54] K. Shimoda, H. Sugaya, M. Murakami, H. Arai, Y. Uchimoto, Z. Ogumi, *J. Electrochem. Soc.* **2014**, *161*, A1012.
[55] J. Popovic, R. Demir-Cakan, J. Tornow, M. Morcrette, D. S. Su, R. Schlögl, M. Antonietti, M. M. Titirici, *Small* **2011**, *7*, 1127.
[56] S. Stegmaier, R. Schierholz, I. Povstugar, J. Barthel, S. P. Rittmeyer, S. Yu, S. Wengert, S. Rostami, H. Kungl, K. Reuter, R. A. Eichel, C. Scheurer, *Adv. Energy Mater.* **2021**, *11*, 2100707.
[57] E. Zhao, F. Ma, Y. Guo, Y. Jin, *RSC Adv.* **2016**, *6*, 92579.
[58] R. A. Huggins, *Ionics (Kiel)* **2002**, *8*, 300.
[59] A. West, J. Irvine, D. Sinclair, *Adv. Mater.* **1990**, *2*, 132.
[60] S. Breuer, D. Prutsch, Q. Ma, V. Epp, F. Preishuber-Pfï, F. Tietz, M. Wilkening, *J. Mater. Chem. A* **2015**, *3*, 21343.
[61] Q. Ma, C. L. Tsai, X. K. Wei, M. Heggen, F. Tietz, J. T. S. Irvine, *J. Mater. Chem. A* **2019**, *7*, 7766.
[62] S. Y. Chung, J. T. Bloking, Y. M. Chiang, *Nat. Mater.* **2002**, *1*, 123.
[63] M. J. Wang, J. B. Wolfenstine, J. Sakamoto, *Adv. Funct. Mater.* **2020**, *30*, 1909140.
[64] J. Liu, T. Liu, Y. Pu, M. Guan, Z. Tang, F. Ding, Z. Xu, Y. Li, *RSC Adv.* **2017**, *7*, 46545.
[65] E. Zhao, F. Ma, Y. Jin, K. Kanamura, *J. Alloys Compd.* **2016**, *680*, 646.
[66] C. A. J. Fisher, V. M. H. Prieto, M. S. Islam, *Chem. Mater.* **2008**, *20*, 5907.
[67] M. Weiss, F. J. Simon, M. R. Busche, T. Nakamura, D. Schröder, F. H. Richter, J. Janek, *Electrochem. Energy Rev.* **2020**, *3*, 221.
[68] V. S. Saji, Y. S. Kim, T. H. Kim, J. Cho, H. K. Song, *Phys. Chem. Chem. Phys.* **2011**, *13*, 19226.
[69] M. Srout, K. Lasri, M. Dahbi, A. Kara, L. Tetard, I. Saadoune, *J. Power Sources* **2019**, *435*, 226803.
[70] Y. Amiki, F. Sagane, K. Yamamoto, T. Hirayama, M. Sudoh, M. Motoyama, Y. Iriyama, *J. Power Sources* **2013**, *241*, 583.
[71] T. V. S. L. Satyavani, B. Ramya Kiran, V. Rajesh Kumar, A. Srinivas Kumar, S. V. Naidu, *Eng. Sci. Technol. Int. J.* **2016**, *19*, 40.
[72] Y. C. Chang, C. T. Peng, I. M. Hung, *J. Mater. Sci.* **2014**, *49*, 6907.
[73] A. Banday, M. Ali, R. Pandey, S. Murugavel, *Phys. Chem. Chem. Phys.* **2019**, *21*, 9858.
[74] H. Wang, A. Lai, D. Huang, Y. Chu, S. Hu, Q. Pan, Z. Liu, F. Zheng, Y. Huang, Q. Li, *New J. Chem.* **2021**, *45*, 5695.
[75] S. Lou, Q. Liu, F. Zhang, Q. Liu, Z. Yu, T. Mu, Y. Zhao, J. Borovilas, Y. Chen, M. Ge, X. Xiao, W. K. Lee, G. Yin, Y. Yang, X. Sun, J. Wang, *Nat. Commun.* **2020**, *11*, 5700.
[76] W. Zhang, D. A. Weber, H. Weigand, T. Arlt, I. Manke, D. Schröder, R. Koerver, T. Leichtweiss, P. Hartmann, W. G. Zeier, J. Janek, *ACS Appl. Mater. Interfaces* **2017**, *9*, 17835.
[77] H. Tan, J. Dodd, B. Fultz, *ECS Trans.* **2019**, *19*, 19.
[78] J. chao Zheng, X. hai Li, Z. xing Wang, J. hui Li, L. jun Li, L. Wu, H. jun Guo, *Ionics (Kiel)* **2009**, *15*, 753.
[79] N. J. J. De Klerk, M. Wagemaker, *ACS Appl. Energy Mater.* **2018**, *1*, 5609.
[80] H. El-Shinawi, A. Regoutz, D. J. Payne, E. J. Cussen, S. A. Corr, *J. Mater. Chem. A* **2018**, *6*, 5296.
[81] H. C. Shin, K. Y. Chung, W. S. Min, D. J. Byun, H. Jang, B. W. Cho, *Electrochem. Commun.* **2008**, *10*, 536.
[82] Y. Koyama, T. Uyama, Y. Orikasa, T. Naka, H. Komatsu, K. Shimoda, H. Murayama, K. Fukuda, H. Arai, E. Matsubara, Y. Uchimoto, Z. Ogumi, *Chem. Mater.* **2017**, *29*, 2855.
[83] L. X. Yuan, Z. H. Wang, W. X. Zhang, X. L. Hu, J. T. Chen, Y. H. Huang, J. B. Goodenough, *Energy Environ. Sci.* **2011**, *4*, 269.
[84] T. Famprikis, P. Canepa, J. A. Dawson, M. S. Islam, C. Masquelier, *Nat. Mater.* **2019**, *18*, 1278.